APPLICATION OF A MEMORY SURFACE MODEL TO PREDICT WHOLE-LIFE SETTLEMENTS OF A SLIDING FOUNDATION

Riccardo Corti. Geotechnical Engineer (former PhD Candidate, Department of Civil Engineering, University of Bristol), Arup, 13 Fitzroy Street, W1T 4BQ, London (corresponding author). E-mail: Riccardo.Corti@arup.com

Susan M. Gourvenec. Professor, Centre for Offshore Foundation Systems, a node of the ARC Centre of Excellence for Geotechnical Science and Engineering, University of Western Australia, 35 Stirling Highway, Crawley, WA 6009, Australia. E-mail: Susan.Gourvenec@uwa.edu.au

Mark F. Randolph. Professor, Centre for Offshore Foundation Systems, a node of the ARC Centre of Excellence for Geotechnical Science and Engineering, University of Western Australia, 35 Stirling Highway, Crawley, WA 6009, Australia. E-mail: Mark.Randolph@uwa.edu.au

Andrea Diambra. Lecturer, Department of Civil Engineering, Queen's Building, University of Bristol, Bristol BS8 1TR, UK. E-mail: Andrea.Diambra@bristol.ac.uk

Paper submitted for possible publication to:

Computers and Geotechnics

Number of words: 5633 (excluding abstract, tables, notation list and references)

Number of figures: 17

Number of tables: 3

ABSTRACT

In this paper a novel modelling procedure is proposed to estimate whole-life settlements of tolerably mobile sliding foundations. A new kinematic hardening-critical state-state parameter constitutive model, the Memory Surface Hardening model, is implemented in a one-dimensional analysis to predict accumulated vertical settlements under drained lateral cyclic loading. The Memory Surface Hardening model performance is compared with the Modified Cam Clay and Severn-Trent Sand models. The Memory Surface Hardening model is adopted to simulate available experimental data from centrifuge tests to predict the settlement of a sliding foundation at the final stable state (i.e. no further volume changes occur).

Keywords: Settlement; cyclic loading; offshore engineering; soil modelling; memory surface.

1 Introduction

Sliding foundations are a novel concept to meet the increasingly challenging demand to limit the footprint of subsea mudmats. In contrast to the traditional paradigm that foundations remain stationary and resist all the applied loads, sliding foundations are designed to move tolerably across the seabed to relieve some of the applied loads, thus requiring a smaller footprint. Sliding displacements are caused, and also limited, by expansion and contraction of attached pipelines ([1], [2], [3]). In general, magnitudes of displacement are sufficient to cause shear failure between the foundation and the soil, where the mobilised ratio of shear stress to normal effective stress is greatest.

Subsea mudmats are shallow, mat-style foundations used to support pipeline infrastructure for offshore hydrocarbon developments. Foundation loads derive from the self-weight of the mat, the supported structure and thermal expansion and contraction of the attached pipelines. Increasing operational loads coupled with softer seabeds has resulted in traditional subsea mudmat designs exceeding the installation capacity of pipelaying vessels. The expense of an additional heavy lift vessel on site to install over-sized mudmats can be prohibitive. Sliding foundations offer a potential solution to this impasse ([1], [2], [3]).

Observations of performance of a sliding foundation on soft clay from a programme of centrifuge model tests are reported by Cocjin et al. [2]. The considered sliding mudmat comprised a rectangular rough-based mat of breadth to length aspect ratio of 0.5 and was provided with edge ‘skis’ to facilitate sliding (rather than overturning that may lead to overstressing of the pipeline connections). A schematic representation of the generalized geometry is presented in Fig. 1, also showing an attached pipeline connection. The tests involved a number of cycles of undrained sliding with intervening periods of consolidation. The model data showed settlement of the mat during each period of consolidation resulting from dissipation of shear induced pore pressures generated during the preceding sliding

event. The accumulated mat settlements reduced with each slide, ultimately reaching a stable state condition with no further volume change in the soil. This stable state was shown to be equivalent to the drained state [4].

This last observation is illustrated in Fig. 2, through an analysis of a strain-imposed cyclic simple shear test under constant total vertical stress conditions using the Modified Cam Clay model [5]. Results compare the stress-volume changes under drained cycles of loading and undrained cycles of loading with intervening periods of consolidation. It is evident that the volumetric behaviours are comparable and the final stable state from the two simulations converge. A further check is performed by comparing the variation of the void ratio with the number of cycles for the performed simulations. The trends are similar, which confirms that the soil response is comparable.

It can therefore be surmised that consideration of drained sliding and associated (drained) volumetric strain is an appropriate approximation for undrained generation and subsequent dissipation of shear induced excess pore pressures. On this assumption, this study investigates the volumetric response of drained lateral cyclic loading of a sliding foundation. Three constitutive models are adopted to estimate vertical settlements over the whole-life of a sliding foundation; predicted results are compared with available data from centrifuge tests performed at the University of Western Australia – Centre for Offshore Foundation Systems (UWA-COFS) [2].

2 Analysis set up and soil model

2.1 Analysis set up

The framework of the 1-D analyses considering a sliding mudmat of width B resting on half-space soil is shown in Fig. 3. The overall soil response under the shearing imposed by the sliding mudmat is computed through a layer-by-layer summation, by dividing the half-space soil domain into n different layers of thickness h_i, where i is the layering index, up to the depth of influence of the loading imposed by the sliding mudmat. The average response of the individual layer i is computed at a characteristic soil element located at its vertical mid-point, as shown in Fig. 3. Since the large stress gradient in the layers close to the foundation base may affect the accuracy of layer-average based procedure, it is customary to use thinner layering in the uppermost layers. The loading conditions in each layer was approximated using available elastic solutions for vertical and shear load distribution with depth [6], while the soil response was computed assuming the three specific elasto-plastic constitutive models outlined above (and described in detail below). Comparison of the shear stress distribution beneath a surface foundation under horizontal sliding in an elasto-plastic medium determined from a finite element analysis (described in [7]) showed adoption of an elastic shear stress distribution to be an appropriate simplification (Figure 4). Each elasto-plastic model was coded in Matlab and solved incrementally using the fourth order Runge-Kutta numerical integration method.

2.2 Constitutive soil models

Three soil constitutive models were used to predict the accumulated settlement during drained lateral cyclic loading: the Modified Cam Clay model (MCC) [5], the Severn-Trent Sand model (STS) [8-9] and the Memory Surface Hardening model (MSH) [10-12], which are represented schematically in Fig. 5. All the three elasto-plastic models assume isotropic elastic laws and are constructed within the framework of Critical State Soil Mechanics

[13,14]. The critical state is modelled as a straight line in the void ratio-mean effective pressure semi-logarithmic plane (e-ln p'). The deviatoric section of all the yield surfaces follows the shape proposed by Argyris et al. (1974) [15] which avoids the presence of singularities and ensures that the critical state strength varies with the Lode angle. The main differences between the models are: a) the shape of the model surfaces in the q-p' plane, which are ellipses for the MCC and wedges for the other two models (STS and MSH), b) the adopted dilatancy rule (defined by d in Fig. 5) and, most importantly, c) the number of model surfaces (defined by their slope η in Fig. 5) which increases from the simplest MCC model using only a yield surface, to the most sophisticated MSH model, which postulates the existence of yield, bounding and memory surfaces. The larger number of model surfaces implies an increased complexity of the employed hardening rule which can allow a more accurate simulation of the non-linear stress and density dependent behaviour of soil as well as the influence of past stress history. This last aspect is expected to be the most important to accurately predict the cyclic response of the sliding mudmat in the following analyses. A brief description of each of the three soil models is provided in the following alongside schematic representations in Fig. 5. The most fundamental mathematical relationships are also reported in Table 1. The full mathematical formulation for each model can be found in the relevant referenced literature as referenced below.

Modified Cam Clay (MCC) model [5]: An elasto-plastic model that assumes an elliptical yield locus that passes through the origin of the stress plane and bounds soil elastic states (Fig. 5a). The size of the yield locus is governed by the parameter p_c. Under elasto-plastic loading conditions, the yield locus evolves preserving its shape and its intersection with the origin of the stress state axis, with the consequent variation in size of the elastic region. An associative flow rule is assumed.

Severn-Trent Sand (STS) model [8,9]: A kinematic hardening – bounding surface elasto-plastic constitutive model. A purely elastic region is bounded by the yield surface (f_Y) which is an open wedge with its apex at the origin of the q-p' stress axes (Fig. 5b) and moves in the stress space (kinematic hardening) under shearing. The bounding surface (f_B) represents the current soil strength and its size is influenced by the current soil density through the state parameter [16]. Based on the bounding surface theory [17,18], plastic soil stiffness is assumed to depend on the distance between the current stress state $\boldsymbol{\sigma}$ and the conjugate one on the bounding surface $\boldsymbol{\sigma}^{\boldsymbol{B}}$, as shown in Fig. 5 (b) and in Table 1. Upon unloading-reloading, the soil response is initially fully elastic inside the yield surface but elasto-plastic conditions are invoked when the opposite boundary of the yield locus is reached.

Memory Surface Hardening (MSH) model [10-12]*:* A recently developed constitutive model based on an extension of the STS model by introducing an additional surface, the memory surface (f_M), which retains information of the recent stress history (Fig. 5c). The memory surface bounds a region of stress states that the soil has already experienced. When the current stress state lies inside the memory surface, the memory surface f_M acts as an additional bounding surface so that the plastic soil modulus is governed by an additional hardening term depending on the distance between the current stress ($\boldsymbol{\sigma}$) state and its projection on the memory surface ($\boldsymbol{\sigma}^{\boldsymbol{M}}$). This results in a stiffer soil behaviour during repeated loading compared with virgin loading conditions. The memory surface can evolve in size and translate in the stress space according to three rules:

Rule 1: Changes in size of the memory surface are linked to plastic strains;

Rule 2: The current stress state must always lie inside or on the boundary of the memory surface;

Rule 3: The yield locus must always be enclosed within the memory surface.

Table 1: Summary of functions used in the selected constitutive models

	Modified Cam Clay [5]	**Severn-Trent Sand [8,9]**	**Memory Surface Hardening [10, 12]**
Yield surface	$f_Y = \frac{q^2}{M^2} + p'(p' - p_c)$	$f_Y = q - \eta^Y p'$	$f_Y = q - \eta^Y p'$
Bounding surface	$---$	$f_B = q - \eta^B p'$	$f_B = q - \eta^B p'$
Memory surface	$---$	$---$	$f_M = q - \eta^M p'$
Flow rule	$d = \frac{M^2 - \eta^2}{2\eta}$	$d = A_d[(1 + k_d)M - \eta]$	$d = A_d[(1 + k_d)M - \eta]$
Hardening modulus	$H = p'\left(\frac{vp'_c}{\lambda - \kappa}\right)(2p' - p'_c)$	$H = \frac{b^2}{b_{max}\beta}$	$H = \frac{b^2}{b_{max}\beta} exp\left[\frac{\mu(1-k\psi)b^M}{b}\left(\frac{p'}{p_{ref}}\right)^{0.5}\right]$

The hardening modulus H presented in Table 1 is introduced to calculate the elasto-plastic stiffness matrix. Following [8,9], this is calculated as

$$\boldsymbol{D}^{ep} = \boldsymbol{D}^{e} - \frac{\boldsymbol{D}^{e}\boldsymbol{m}\,\boldsymbol{n}^{T}\boldsymbol{D}^{e}}{\boldsymbol{n}^{T}\boldsymbol{D}^{e}\boldsymbol{m} + H} \quad (1)$$

Where $\boldsymbol{D}^e$ is the elastic stiffness matrix, $\boldsymbol{n}$ is the normal outwards from the yield surface and $\boldsymbol{m}$ is the normal outwards from the plastic potential surface. An exhaustive description of the terms is provided in [8,9] and [12]. It should be noted the slightly different formulation of the hardening modulus of the Memory Surface Hardening model from the one defined in [10-12], where the dependence on the ratio $(p'/p_{ref})^{0.5}$ is inspired by the previous work from Hardin and Black [19] and it accounts for the influence of the effective mean stress. The quantity b

141 represents the distance between the current stress state ($\boldsymbol{\sigma}$) and the image stress on the
142 bounding surface ($\boldsymbol{\sigma}^{\boldsymbol{B}}$) with b_{max} its maximum value, the quantity b^M is the distance between
143 the current stress state ($\boldsymbol{\sigma}$) and the image on the memory surface ($\boldsymbol{\sigma}^{\boldsymbol{M}}$), ψ is the state
144 parameter, p' is the effective mean pressure, p_{ref} is a reference pressure (p_{ref} = 100 kPa) and μ
145 and β are two constitutive parameters. The constitutive parameters β and μ are quite relevant
146 for this application because they govern the magnitude of the accumulated strains during the
147 first slide and under cyclic loading conditions, respectively. It should be noted that by
148 imposing the parameter $\mu=0$, the hardening modulus of the STS is re-established.
149

150 ## 3 Calibration of the constitutive parameters

151 Summary and description of the constitutive parameters for the three models considered are
152 provided in Table 2. The number of constitutive parameters required by the models is
153 proportional to their complexity - 5, 10 and 12 for the MCC, STS and MSH respectively –
154 but, as shown in Table 2, the fundamental parameters are shared and the increased
155 complexity is reflected only in the use of additional parameters. For consistency in the
156 following analysis, the shared constitutive parameters must also assume the same value for
157 the different models employed. The calibrated numerical values of the model parameters are
158 also provided in Table 2. The first five constitutive parameters in Table 2 are shared by all
159 three models and have been calibrated in accordance with Stewart [20] and Acosta-Martinez
160 and Gourvenec [21], who used the MCC model to simulate the behaviour of exactly the same
161 kaolin clay material used in the centrifuge model tests [2] back-analysed in this paper. Thus,
162 only the calibration procedure for the other constitutive parameters (no. 6 to 12 in Table 2)
163 relative to the STS and MSH models is presented in this section. The constitutive parameters
164 of the STS and MSH models have been calibrated against an available drained cyclic triaxial
165 test on speswhite kaolin clay [22]. Information on the mechanical properties of this material

166 can be found in [23] and shows the kaolin is similar to that used in the centrifuge tests [2].
167 The shared constitutive parameters between the STS and MSH (No. 6 to 10 in Table 2) have
168 been calibrated by fitting the initial virgin behaviour while the constitutive parameter μ has
169 been calibrated by fitting the experimental data under the subsequent cyclic conditions. The
170 damage parameter ς of the MSH model governing an eventual damage of the memory surface
171 (f_M) upon dilation is not included because it is not relevant for the very soft soil conditions
172 simulated in this study. The model calibration against an available cyclic drained triaxial test
173 is provided in Fig. 6.

174 **Table 2: Constitutive parameters description.**

Constitutive model			**No.**	**Parameter**	
Memory Surface Hardening model	Severn-Trent Sand model	Modified Cam Clay model	1	κ	0.044
			2	M_{cv}	0.92 (ϕ'=23.5°)
			3	e_{CSL}	2.14
			4	λ	0.205
			5	v	0.3
			6	R	0.05
			7	β	0.017
			8	k^*	1.5
			9	A_d	2.5
			10	k_d	0
			11	μ	11.5
			12	ς	n. r.

175

4 Analysis procedure

In accordance with the centrifuge tests [2], the analyses are referred to a rectangular mudmat of width B = 5 m and aspect ratio B/L= 0.5, where L is the foundation length. The soil beneath the sliding foundation has been discretised in n = 13 soil layers with soil layers thickness being h_i = 0.5 m for the two shallowest layers and h_i = 1 m for the deeper ones. The full loading history of the soil has been considered, including the following three main loading stages:

1) Geostatic stage (soil self-weight consolidation prior to installation of foundation).
2) Foundation set-down stage (consolidation after foundation installation).
3) Foundation sliding stage (cyclic sliding of foundation).

4.1 Geostatic stage

The in situ soil state at the end of soil self-weight consolidation prior to installation of the foundation can be represented as K_0-consolidation process under axisymmetric stress conditions. This will be referred to as condition '*0*' as it represents the initial soil state before installation of the mudmat. Stress variables referring to this condition are denoted by the subscript '$_0$'. The initial in situ vertical effective stress is given by:

$$\sigma'_{v0} = \gamma' z \tag{2}$$

where γ' is the drained unit weight of the kaolin, taken as γ' = 5.7 kN/m^3 [2]. The initial in situ horizontal effective stress is given by:

$$\sigma'_{h0} = K_0 \sigma'_{v0} \tag{3}$$

where K_0 is the lateral earth pressure coefficient given by Jaky's formula [24]:

$$K_0 = 1 - sin\phi' \quad (4)$$

with the critical state friction angle ϕ' as assumed in Table 2.

The initial void ratio is estimated using the MCC model formulation and imposing normally consolidated conditions:

$$e_0 = e_{CSL} - (\lambda - \kappa) \ln \frac{p'_{c0}}{2} - \kappa \ln p'_0 \quad (5)$$

where p'_0 is the current in situ effective mean pressure determined using σ'_{v0} and σ'_{h0}. The quantity p'_{c0} is the pre-consolidation pressure defining the size of the MCC yield locus that can

be derived using the formulation of the yield locus for the MCC model:

$$p'_{c0} = p'_0 + \frac{q_0^2}{p'_0 M^2} \quad (6)$$

where $q_0 = \sigma'_{v0} - \sigma'_{h0}$ is the deviator stress. The estimated initial in situ vertical and horizontal effective stress profiles, σ'_{v0} and σ'_{h0}, and void ratio profile e with depth z are shown in Fig. 7a-b respectively.

4.2 Foundation installation stage

The change in vertical effective stress $\Delta\sigma'_v$ with depth z resulting from placement of the foundation load is approximated with the elastic solution of Poulos & Davis (1974) [6]. The

stress increase below the centre of a rectangular foundation induced by a uniform vertical pressure q_{op} can be expressed as:

$$\Delta\sigma'_v = 2\frac{q_{op}}{\pi}\left[\frac{B}{2A}\left(1+\frac{z^2}{2A^2}\right)\operatorname{atan}\frac{L}{2A}+\frac{L}{2D}\left(1+\frac{z^2}{2D^2}\right)\operatorname{atan}\frac{B}{2D}+\frac{BLz^2}{8C^2}\left(\frac{1}{A^2}+\frac{1}{D^2}\right)\right] \quad (7)$$

where A, B, C, D, L and z are geometrical distances represented schematically in Fig. 8.

A schematic representation of the normalized vertical stress change $\Delta\sigma'_v/q_{op}$ with depth z is represented in Fig. 9a. At this stage, the value of the lateral earth pressure coefficient assumed in Eq. (4) was compared to the stress ratio calculated assuming a horizontal stress change from the elastic solution of Poulos & Davis (1974) [6]. At a normalized depth z/B of 0.1, a difference of 15% was found, with the K_0 value calculated in Eq. (4) being larger than the horizontal stress ratio calculated using the elastic solution. This difference reduced to 10% at a normalised depth $z/B = 0.3$.

The magnitude of the foundation vertical pressure q_{op} is a variable (input) parameter and can be defined as a portion of the available undrained bearing capacity q_u. In field conditions for subsea mudmats on soft clays, the ratio q_{op}/q_u is generally between 0.3 and 0.5 [2]. For consistency with the centrifuge tests [2], the foundation vertical pressure q_{op} is set to satisfy the following condition:

$$q_{op} = 0.3q_u \quad (8)$$

To ensure consistency between the calculated bearing capacity and the constitutive models, the undrained shear strength profile is determined from the assumed elastic and critical state soil properties. Following the procedure outlined in [25], it is possible to determine the

250 undrained shear strength profile using the input parameters of the MCC model as shown in
251 Eqs (9) to (11).

252 $$\frac{s_u}{\sigma'_{v0}} = g(\theta)\cos\theta\,\frac{1+2K_0}{3}\,\left[\frac{(a^2+1)}{2}\right]^{1-\left(\frac{\kappa}{\lambda}\right)} \quad (9)$$

253 where

254 $$g(\theta) = \frac{\sin\phi'}{\cos\theta+\left(\frac{1}{\sqrt{3}}\right)\sin\phi'\sin\theta} \quad (10)$$

255 and

256 $$a = \frac{\sqrt{3}(1-K_0)}{g(-30^\circ)(1+2K_0)} \quad (11)$$

257 The symbol θ is the Lode's angle, taken as 0 to represent plane strain shear strength. The
258 undrained shear strength profile is calculated by assuming the same undrained shear strength
259 at the surface s_{um} = 0.52 kPa as that measured in situ; to do this, an extra overburden stress of
260 1.85 kPa is applied in situ. An undrained shear strength gradient k = 1.70 kPa/m is derived
261 from the critical state properties, giving a dimensionless strength heterogeneity coefficient
262 kB/s_{um} ~ 16. Bearing capacity factors for rectangular foundations are available for soil
263 strength heterogeneity in the range $0 \leq kB/s_{um} \leq 10$ [26], while solutions exist for the
264 appropriate kB/s_{um} but assuming plane strain geometry [27]. The outcome from extrapolating
265 a bearing capacity factor for the rectangular foundation geometry to the appropriate kB/s_{um} for
266 this example is similar to the plane strain solution (approximately 10% lower). For this
267 simulation the operative bearing pressure is taken as
268
269 $$q_{op} = 0.3N_{cV}s_{um} = 0.3(15.85)(0.52\ kPa) = 0.3(8.25\ kPa) = 2.48\ kPa \quad (12)$$
270
271 By introducing the above value of q_{op} in Eq. (7), the increase of vertical stress $\Delta\sigma'_v$ for the
272 characteristic points of each layer i can be determined. Assuming K_0 compression conditions,
273 the Modified Cam Clay model has been employed to determine the vertical strain ε_v^i and the

void ratio e^i at each characteristic point. The overall vertical settlement of the soil can be determined by assuming a constant vertical strain throughout each layer and by summing the contribution of each layer to give:

$$\delta_v = \sum_{i=1}^{n} \varepsilon_v^i \, h^i \tag{13}$$

4.3 Foundation sliding stage

Under operational conditions, the foundation is subjected to forward and backward cyclic sliding. The concept of a sliding mudmat is such that the foundation is free to exceed by far the displacement needed to mobilize the limiting soil-foundation shear resistance to sliding, $\tau_{max.}$. The limiting soil-foundation shear resistance, which represents the (average) shear stress cyclic amplitude which the sliding foundation is subjected to, is found as a proportion of the foundation operative vertical stress q_{op}:

$$\tau_{max} = q_{op} \tan \phi' = 1.08 \, kPa \tag{14}$$

where the friction between the mudmat and the soil is a function of the friction angle tan ϕ', as was also detected in the experimental tests [2]. The shear stress distribution with depth during full sliding can be predicted using the idealized elastic solution for a foundation on a semi-infinite soil mass as a function of the shear stress on the surface τ_{max} [6]:

$$\tau = 2\frac{\tau_{max}}{\pi}\left[\operatorname{atan}\frac{B}{2z} - \frac{z}{D}\operatorname{atan}\frac{B}{2D} + \frac{B}{2z}\left(\frac{B^2}{4A^2} - \frac{B^2+L^2}{4C^2}\right)\right] \tag{15}$$

The distribution of shear stress τ normalized by the interfacial shear stress τ_{max} with depth during sliding is shown in Fig. 9b. The horizontal cyclic loading acting on the foundation has

been reproduced considering equivalent simple shear conditions; the shear stress cyclic amplitude $\Delta\tau^{cyc}$ has been derived from Eq. (15) by assuming $\Delta\tau^{cyc} = \pm \tau$, where the sign ± is implemented to include the direction of the loading cycles (forward or backwards). The simulations of the foundation sliding stage have been performed separately for the three constitutive models (MCC, STS and MSH) in order to investigate their capabilities. A total of 40 back-and-forth cycles have been imposed in order to simulate the long-term behaviour of sliding foundations. The overall foundation settlement for this stage is determined using Eq. (13) above.

5 Analysis results

5.1 Model performances

Comparison of the predicted foundation vertical settlements normalised by the width of the foundation (δ_v/B) during the 40 imposed shearing cycles is presented in Fig. 10a for the MCC model, Fig. 10b the STS model and Fig. 10c for the MSH model. A direct comparison of evolution of the vertical settlements with number of loading cycles is also presented in Fig. 10d. The predicted trends and magnitude of settlements differ considerably among these models. The MCC model predicts a normalized vertical displacement $\delta_v/B = 9 \cdot 10^{-4}$ at the stable state, which is reached at the end of the very first shearing cycle with no further densification occurring with subsequent cycles since the load path lies within the now expanded yield surface (Fig. 10a). On the contrary the STS model predicts a much larger normalised vertical displacement, $\delta_v/B = 1.5 \cdot 10^{-1}$ after 40 cycles (Fig. 10b). In this case, a stable state is not reached as the model does not accurately capture the rate of plastic strain hardening. The prediction of the MSH model lies between the MCC and STS model predictions outlined above, suggesting a normalized vertical displacement $\delta_v/B = 4.4 \cdot 10^{-2}$

after 40 cycles which is gradually reached during the cyclic loading sequence (Fig. 10c). Settlement measured in the centrifuge test [2] is also reported in Fig. 10d for comparison with the three computations performed. It is clear that while the MSH model predicts qualitatively and quantitatively the closest behaviour to the experimental observation, the final vertical displacement of the foundation is slightly underestimated. This may be the result of limitations in the calibration exercise performed for experimental results on soil samples tested under different loading conditions (triaxial compression instead of simple shear) and under much larger confining pressure (up to two orders of magnitude).

Fig. 11 shows a comparison among the predictions of the three models for the settlement during the first slide. The normalized settlement predicted by the MCC model is the lowest among the models, which follows directly from the nature of the model (an isotropic hardening model). Moreover, the development of the vertical settlements is interrupted by the initial expansion of the yield surface, which occurs at $N_{cyc} = 0.5$ (representing the first half of the foundation slide). The vertical settlements predicted by the STS and MSH models at $N_{cyc} = 0.5$ are similar and the small difference is due to the slightly different hardening rule implemented in the models. During the first half loading cycle the soil stiffness in the two models is governed by the constitutive parameter β. At $N_{cyc} = 1$, the difference in the simulated vertical settlement increases as the dependence on the memory surface in the MSH model is activated leading to an increase in the plastic soil stiffness which inevitably reduces the magnitude of predicted vertical settlements. The plastic soil stiffness in the MSH model is now governed by the constitutive parameters β and μ.

The difference between the three computations can be understood by analysing the predicted behaviours (Fig. 12), stress paths and evolutions of the yield surfaces (Fig. 13), and void ratio changes (Fig. 14) for the shallowest soil element considered. This soil element is indeed that subjected to the largest shear stress cycles and in turn shows the largest vertical strains.

The observed immediate achievement of the stable state for the MCC model is the result of the isotropic hardening expansion of the yield surface upon the first shearing cycle and the resulting fully elastic behaviour during the following shearing cycles imposed within the purely elastic region bounded by the yield surface (Fig. 12a and Fig. 13a). As expected no changes in void ratio are recorded after the first cycle, as shown in Fig. 14a.

The very large settlements predicted using the STS model (Fig. 12b) are the result of the imposed kinematic hardening to the yield surface and the lack of any mechanism to record that the soil has been subjected to the same shearing conditions in previous cycles. In fact, during cyclic shearing, the yield surface moves up and down kinematically as shown in Fig. 13b and the only difference between subsequent cycles is a slight expansion of the bounding surface caused by the progressive soil densification. The plastic soil stiffness, which is affected by the distance between the current stress state and the image stress on the bounding surface (the quantity b in Fig. 5b), only slightly increases during cyclic shearing and a stable state cannot be reached. Actually, the soil continues to compress indefinitely to reach unreasonable values such as a vertical strain $\varepsilon_v = 1.00$. The soil would continue to compress unrealistically if further cyclic shearing were to be imposed.

The response of the MSH model lies in between the MCC and STS model responses as shown by the stress-strain behaviour in Fig. 12c. For this model, the yield surface still moves up and down kinematically as shown for the STS model in Fig. 13b, but the introduction of an evolving memory surface (shown in Fig. 13c) allows the progressive stiffening during repeated loading to be captured. One can interpret the memory surface as a record of the current fabric of the soil, describing the range of stresses that can be imposed without major disruptions to particle arrangement. Thus, the memory surface bounds a region of increased stiffness and its progressive increase during cyclic shearing allows a progressive increase of the plastic soil stiffness. In this case a stable state is gradually reached with increased number

374 of cycles. Similarly to the STS model, the MSH model predicts a compression of the soil
375 element to a void ratio well below the critical state line (Fig. 14c) but the progressive soil
376 stiffening prevents the soil from reaching inadmissible states. The independency of the soil
377 volumetric response from the corresponding critical state value during cyclic loading has
378 been confirmed experimentally by several studies on granular soils (e.g. [28-29]). It should
379 also be noted that the response of the STS and MSH model during the first shearing cycle are
380 similar and the additional memory surface of the MSH model affects only the soil behaviour
381 under unloading-reloading conditions.
382 Among the three analyses, the computation using the MSH model is the only one
383 qualitatively similar to the experimental results obtained by Cocjin et al. [2] with a stable
384 state reached progressively during cyclic loading. Using material parameters and boundary
385 conditions available in the literature [2, 22], a reasonable quantitative fit to observed
386 experimental results [2] is also achieved with the MSH model.
387

388 **5.2 Sensitivity analysis of MSH model hardening parameter, μ**

389 In this section a numerical exercise is provided to assess the sensitivity of the MSH model
390 parameter, μ. This parameter affects the magnitude of the soil hardening modulus, thus of soil
391 stiffness, when the stress state lies within the memory surface. The larger the parameter, the
392 stiffer the soil response under cyclic loading but the slower the expansion of the memory
393 surface during progressive cycles. If this parameter is set to zero the STS model is recovered.
394 Fig. 15 indicates the effect of varying the constitutive parameter μ, introduced in Eq. (1), and
395 shows that the predicted vertical settlement at the stable state increases by decreasing the
396 value of the parameter μ. The results from the three simulations are compared directly in Fig.
397 15d where the accumulated vertical displacements are plotted against the number of cycles;
398 the final displacement measured experimentally by Cocjin et al. [2] is also shown and it

399 seems that a value of the parameter $\mu = 8$ provides a good fit to the final displacement at the
400 stable state. It should be noted that the value that fits the experimental data ($\mu = 8$) is quite
401 close to that obtained from the model calibration exercise ($\mu = 11.5$).
402 The foundation set-down settlement is well reproduced by the numerical analysis;
403 experimentally the measured settlement is 0.081 m while the calculated settlement from the
404 simulation is 0.077 m; the foundation set-down displacement is calculated using the MCC
405 model and assuming K_0-consolidation conditions.
406 Using the best-fit simulation to the experimental data it is possible to analyse the predicted
407 trend of void ratio and settlement with depth. Fig. 16a presents the profile of void ratio with
408 normalized depth predicted at the end of the three stages (geostatic, foundation set-down and
409 cyclic shearing), while Fig. 16b presents the trends of displacement δ_v normalised by the
410 width of the foundation B for each loading stage. From Fig. 16b, it is clear that while the
411 foundation set-down induces less settlement in the soil than the cyclic shearing stage, it
412 affects layers to a greater depth. The foundation set-down stage affects deeper soil layers and
413 this is confirmed by the percentage of vertical displacements (72%) occurring within a depth
414 of 0.5B. By contrast, the cyclic shearing stage appears to be a very superficial mechanism
415 which just affects the soil to a maximum depth of 0.5B; in fact almost 100% of vertical
416 settlements take place in the top 3 m of soil (0.6B). These findings are related to the stress
417 distribution from the assumed elastic solution for the foundation set-down stage (Fig. 9a) and
418 the sliding stage (Fig. 9b). The zone of influence of horizontal cyclic loading is predicted to
419 be limited to a depth of approximately half the foundation breadth, in good agreement with
420 the experimental results [2].

421 # 6 Parametric study

422 In this section a parametric study is presented to assess the effect on whole-life settlement of
423 sliding foundations after 40 lateral loading cycles as a function of soil strength heterogeneity

and foundation aspect ratio. The simulations were undertaken using the Memory Surface Hardening model calibrated using the input values given in Table 2, but with the best-fit hardening value presented above (μ = 8). The strength properties, overburden stresses and foundation weights considered in the parametric study are summarised in Table 3. The soil strength properties were obtained using Eqs. (9) to (11), imposing the Modified Cam-Clay constitutive parameters presented in Table 2 and changing the overburden stress. Figure 17 (a) shows the long term normalised foundation settlement with the number of cycles of sliding on soils with different undrained shear strength profiles. Shear strength profiles of kB/s_{um} = 0, 20 and 100 were assumed in this assessment. The vertical displacement after 40 cycles seem rather comparable for a shear strength profile of kB/s_{um} = 20 and 100, where after 40 cycles a normalised displacement of 0.058 and 0.055 is calculated. The normalised displacement for a soil strength kB/s_{um} = 0 is rather limited as a consequence of the large overburden stress, which implies significant soil compression during the foundation set down stage, as shown in Table 3. Figure 17 (b) shows the accumulated normalised vertical displacement of sliding foundations with different aspect ratio *B/L*. The simulations show that the accumulated normalised displacement increases as the aspect ratio *B/L* decreases.

Table 3: Soil parameters for parametric study of Figure 17 (a)

kB/s_{um}	s_{um} (kPa)	k (kPa/m)	Overburden stress, $\Delta\sigma'_v$ (kPa)	q_{op} (kPa)
0	112	2.2	400	195
20	0.42	1.7	1.50	2.18
100	0.08	1.67	0.30	1.27

7 Conclusions

In this paper a numerical procedure has been proposed to estimate the whole-life settlements of tolerably mobile subsea foundations under cycles of horizontal shearing. The approach is based on the validated assumption that a drained soil response is an appropriate proxy for alternating stages of undrained sliding and consolidation.

A one-dimensional model was developed to represent stress and volume changes beneath a mat foundation.

Three different constitutive models were used to simulate the soil response to the whole life operation of a sliding foundation: the Modified Cam Clay model, the Severn-Trent Sand model and the Memory Surface Hardening model. Initially the models were calibrated against a drained cyclic triaxial test available in the literature. The Modified Cam Clay model was adopted to simulate the soil consolidation and the foundation set-down stages, assuming K_0-consolidation stress path. The foundation sliding stage was then performed by simulating 40-cycles of simple shear; the three constitutive models were adopted to calculate the vertical settlements of the foundation. The Severn-Trent Sand model struggled to reproduce the typical stable state that is observed in soils under cyclic loading conditions while the Modified Cam Clay model predicted just elastic strains under drained cyclic loading. The Memory Surface Hardening model was able to reproduce both plastic deformations under cyclic loading and an approach to the stable state.

The following aspects were observed:

- The vertical displacement related to the foundation set-down stage could be well reproduced by the Modified Cam Clay Model.

- The maximum density condition (at the steady state) could be well predicted by the Memory Surface Hardening model but not the Modified Cam Clay Model and Severn Trent Sand models.
- The numerical analysis confirmed that the foundation sliding mechanisms influences just the near surface soil.

The Memory Surface Hardening model was demonstrated to successfully calculate the vertical settlements of a sliding foundation on normally consolidated kaolin clay when compared with results from an available centrifuge test. The model applicability should be investigated further for different foundation and soil conditions before being applied outside the conditions considered in this study. Nonetheless, the study has indicated that this class of model has the potential to capture the essential components of whole-life settlements of tolerably mobile subsea foundations through the assumption that a drained soil response is an appropriate proxy for alternating stages of undrained sliding and consolidation.

8 Acknowledgments

This work forms part of the activities of the Centre for Offshore Foundation Systems (COFS), currently supported as a node of the Australian Research Council's Centre of Excellence for Geotechnical Science and Engineering, and through the Fugro Chair in Geotechnics, the Lloyd's Register Foundation Chair and Centre of Excellence in Offshore Foundations and the Shell EMI Chair in Offshore Engineering.
The work was carried out while the first author was a visiting scholar at COFS, supported through the Worldwide University Network (WUN) Research Mobility Program.

The second author is supported through ARC grant CE110001009 and third author through the Fugro Chair in Geotechnics. The work presented in this paper was supported by ARC grant DP140100684. All financial support is gratefully acknowledged.

The authors are grateful to Dr. Xiaowei Feng for providing the finite element analysis validation of the shear stress distribution.

9 Notation list

Symbol	Description
A	Geometrical distance to calculate the stress distribution beneath the foundation
A_d	Flow rule multiplier
B	Foundation width
C	Geometrical distance to calculate the stress distribution beneath the foundation
D	Geometrical distance to calculate the stress distribution beneath the foundation
L	Foundation length
b	Distance between the current stress state $\boldsymbol{\sigma}$ and the conjugate one on the bounding surface $\boldsymbol{\sigma}^{\boldsymbol{B}}$
b^M	Distance between the current stress state $\boldsymbol{\sigma}$ and the conjugate one on the memory surface $\boldsymbol{\sigma}^{\mathbf{M}}$
b_{max}	Maximum value of b
β	Parameter controlling the amount of settlement in the first slide
d	Dilatancy flow rule
δ_v	Vertical displacement
e	Void ratio

e_{CSL}	Intercept of the critical state line in e-ln p' space at p'=1 kPa
ε_v	Vertical strain
f_Y	Yield surface
f_B	Bounding surface
f_M	Memory surface
h	Layer thickness
H	Hardening modulus
k	Undrained shear strength gradient
k^*	Parameter controlling the relationship between state parameter and available strength
k_d	Stress-dilatancy parameter
k_0	Lateral earth pressure
M_{cv}	Critical state stress ratio for compression
N_{cV}	Bearing capacity factor
N_{cyc}	Number of cycles
p'	Effective mean stress
p'_c	Consolidation pressure
p_{ref}	Reference pressure (=100 kPa)
q	Deviatoric stress
q_{op}	Foundation vertical pressure
q_u	Ultimate bearing capacity
R	Ratio of sizes of yield surface and bounding surface
s_{um}	Undrained shear strength at the surface

z	Depth
γ'	Effective unit weight
η	Stress ratio
κ	Slope of re-compression line in the e-ln p' space
λ	Slope of the critical state line in e-ln p' space
μ	Constitutive parameter affecting the MSH model response in cyclic conditions
v	Poisson's ratio
$\boldsymbol{\sigma}$	Stress state
$\boldsymbol{\sigma^B}$	Conjugate stress point on the bounding surface
$\boldsymbol{\sigma^M}$	Conjugate stress point on the memory surface
σ'_v	Effective vertical stress
ς	Constitutive parameter affecting the contraction of the memory surface
τ_{max}	Maximum shear stress under cyclic loading
ψ	State parameter
$\Delta\tau_{cyc}$	Cyclic amplitude in each soil layer

10 References

[1] Cathie, D., Morgan, N. & Jaeck, C. Design of sliding foundations for subsea structures. In: Brown Editor. BGA International Conference on Foundation. Dundee; 2014. pp. 24-27.

[2] Cocjin M, Gourvenec S, White DJ, Randolph M. Tolerably mobile subsea foundations – observations of performance. Géotechnique 2014;64(11):895-909. DOI: 10.1680/geot.14.P.098

505 [3] Deeks A, Zhou H, Krisdani H, Bransby F, Watson P. Design of direct on-seabed sliding
506 foundations. In: Proceedings of the ASME 2014 33rd International Conference on Ocean,
507 Offshore and Arctic Engineering. San Francisco; 2014. p. V003T10A024. DOI:
508 10.1115/OMAE2014-24393
509 [4] Cocjin M, Gourvenec S, White DJ, Randolph M. Effects of drainage on the response of a
510 sliding foundation. In: Meyer Editor. Frontiers in Offshore Geotechnics III. London: Taylor
511 & Francis Group; 2015. p.777-82. DOI: 10.13140/RG.2.1.2621.4561
512 [5] Roscoe KB, Burland JB. On the generalised stress-strain behaviour of 'wet clay'. In.
513 Heyman, Leckie editors. Engineering Plasticity. Cambridge: Cambridge University Press.
514 1968; p. 535-609.
515 [6] Poulos HG, Davis EH. Elastic Solutions for Soil and Rock Mechanics. New York: John
516 Wiley & Sons Inc; 1974.
517 [7] Feng X, Gourvenec S.M. Modelling sliding resistance of tolerably mobile subsea
518 mudmats. Géotechnique 2016;66(6):1-10. DOI: 10.1680/jgeot.15.P.178
519 [8] Gajo A, Muir Wood D. Severn-Trent sand: a kinematic-hardening constitutive model: the
520 q-p formulation. Géotechnique 1999;49(5):595-614. DOI: 10.1680/geot.1999.49.5.595
521 [9] Gajo A, Muir Wood D. A kinematic hardening constitutive model for sands: the
522 multiaxial formulation. International Journal for Numerical and Analytical Methods in
523 Geomechanics 1999;23(9):925-65. DOI: 10.1002/(SICI)1096-
524 9853(19990810)23:9<925::AID-NAG19>3.0.CO;2-M
525 [10] Corti R, Diambra A, Nash DFT, Muir Wood D. An evolving memory surface for
526 modelling the cyclic behaviour of granular soils. In: Manzanal, Sfriso, editors. Proceedings
527 of the XV Panamerican Conference on Soil Mechanics and Geotechnical Engineer. Buenos
528 Aires (Argentina); 2015. DOI: 10.3233/978-1-61499-603-3-1001

529 [11] Corti R, Diambra A, Escribano DE, Nash DFT, Muir Wood D. A memory surface
530 hardening model for granular soils under repeated loading conditions. Journal of Engineering
531 Mechanics 2016;142(12). DOI: 10.1061/(ASCE)EM.1943-7889.0001174
532 [12] Corti R. Hardening memory surface constitutive model for granular soils under cyclic
533 loading conditions. PhD Thesis University of Bristol; 2016.
534 [13] Roscoe KH, Schofield AN, Wroth CP. On the Yielding of Soils. Géotechnique
535 1958;8(1):22-53. DOI: 10.1680/geot.1958.8.1.22
536 [14] Muir Wood D. Soil behaviour and critical state soil mechanics. Cambridge University
537 Press; 1990.
538 [15] Argyris JH, Faust G, Szimmat J, Warnke EP, Willam KJ. Recent developments in the
539 finite element analysis of prestressed concrete reactor vessels. Nuclear Engineering and
540 Design 1974;28(1):42-75. DOI: 10.1016/0029-5493(74)90088-0
541 [16] Been K, Jefferies M. A state parameter for sands. Géotechnique. 1985;35(1):99-112.
542 DOI: 10.1680/geot.1985.35.2.99
543 [17] Dafalias YF, Popov EP. A model of nonlinearly hardening materials for complex
544 loading. Acta Mechanica. 1975;21(3):173-92. DOI: 10.1007/BF01181053
545 [18] Dafalias YF. Bounding surface plasticity. Part I: Mathematical foundation and
546 hypoplasticity. Journal of Engineering Mechanics. 1986;112(9):966-87. DOI:
547 10.1061/(ASCE)0733-9399(1986)
548 [19] Hardin BO, Black WL. Sand stiffness under various triaxial stresses. Journal of the Soil
549 Mechanics and Foundation Division 1966;92(SM2):27-42.
550 [20] Stewart DP. Lateral loading of piled bridge abutments due to embankment construction.
551 PhD Thesis University of Western Australia; 1992.

552 [21] Acosta-Martinez HE, Gourvenec SM. One-dimensional consolidation tests on kaolin
553 clay. In: Research Report GEO:06385, Centre for Offshore Foundation Systems, School of
554 Civil and Resource Engineering, the University of Western Australia; 2006.
555 [22] Al-Tabbaa A. Permeability and stress-strain response of Speswhite kaolin. PhD Thesis
556 University of Cambridge; 1987.
557 [23] Al-Tabbaa A, Muir Wood D. Some measurements of the permeability of kaolin.
558 Géotechnique. 1987:37(4):499-503. DOI: 10.1680/geot.1987.37.4.499
559 [24] Jaky J. Pressure in silos. In: Proceedings of the 2nd International Conference on Soil
560 Mechanics and Foundation Engineering. London; 1948. p. 103-7.
561 [25] Potts, D.M. & Zdravkovic, L. Finite element analysis in geotechnical engineering -
562 theory. London, UK: Thomas Telford.
563 [26] Feng X, Randolph MF, Gourvenec S, Wallerand R. Design approach for rectangular
564 mudmats under fully three dimensional loading, Géotechnique 2014;64(1):51-63. DOI:
565 10.1680/geot.13.P.051
566 [27] Davis EH, Booker JR. The effect of increasing strength with depth on the bearing
567 capacity of clays. Géotechnique 1973;23(4):551-63. DOI: 10.1680/geot.1973.23.4.551
568 [28] Lopez-Querol S, Coop MR. Drained cyclic behaviour of loose Dogs Bay sand.
569 Géotechnique 2012;62(4):281-9. DOI: 10.1680/geot.8.P.105
570 [29] Escribano D. Evolution of stiffness and deformation of Hostun Sand under drained
571 cyclic loading. PhD Thesis University of Bristol; 2014.
572
573

Figure 1

Click here to download high resolution image

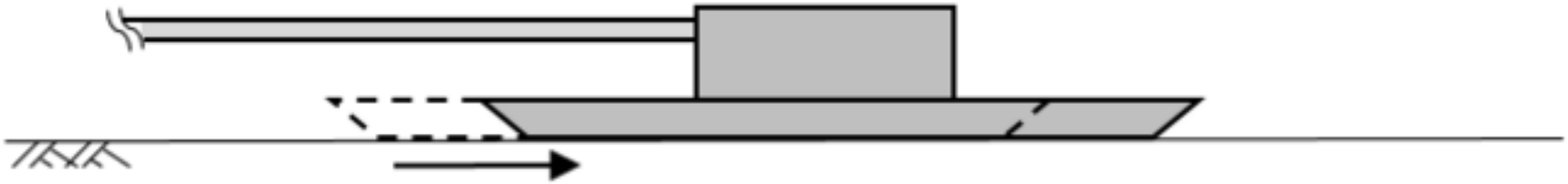

Figure 2
Click here to download high resolution image

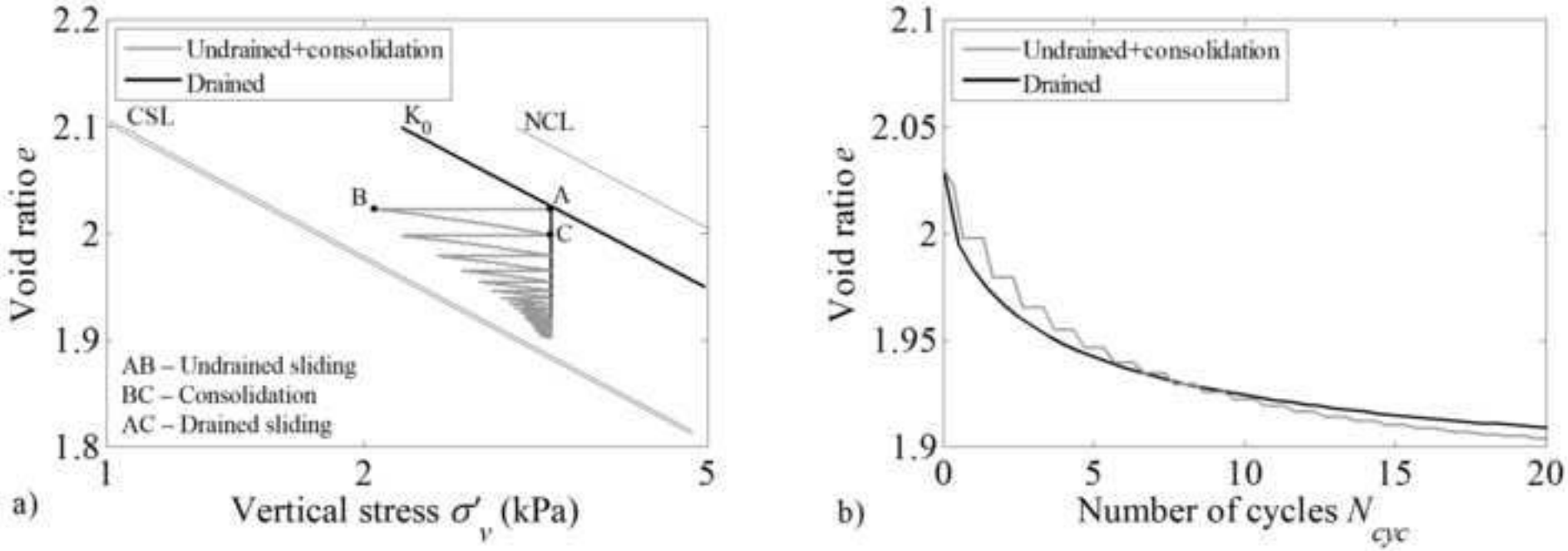

Figure 3

Click here to download high resolution image

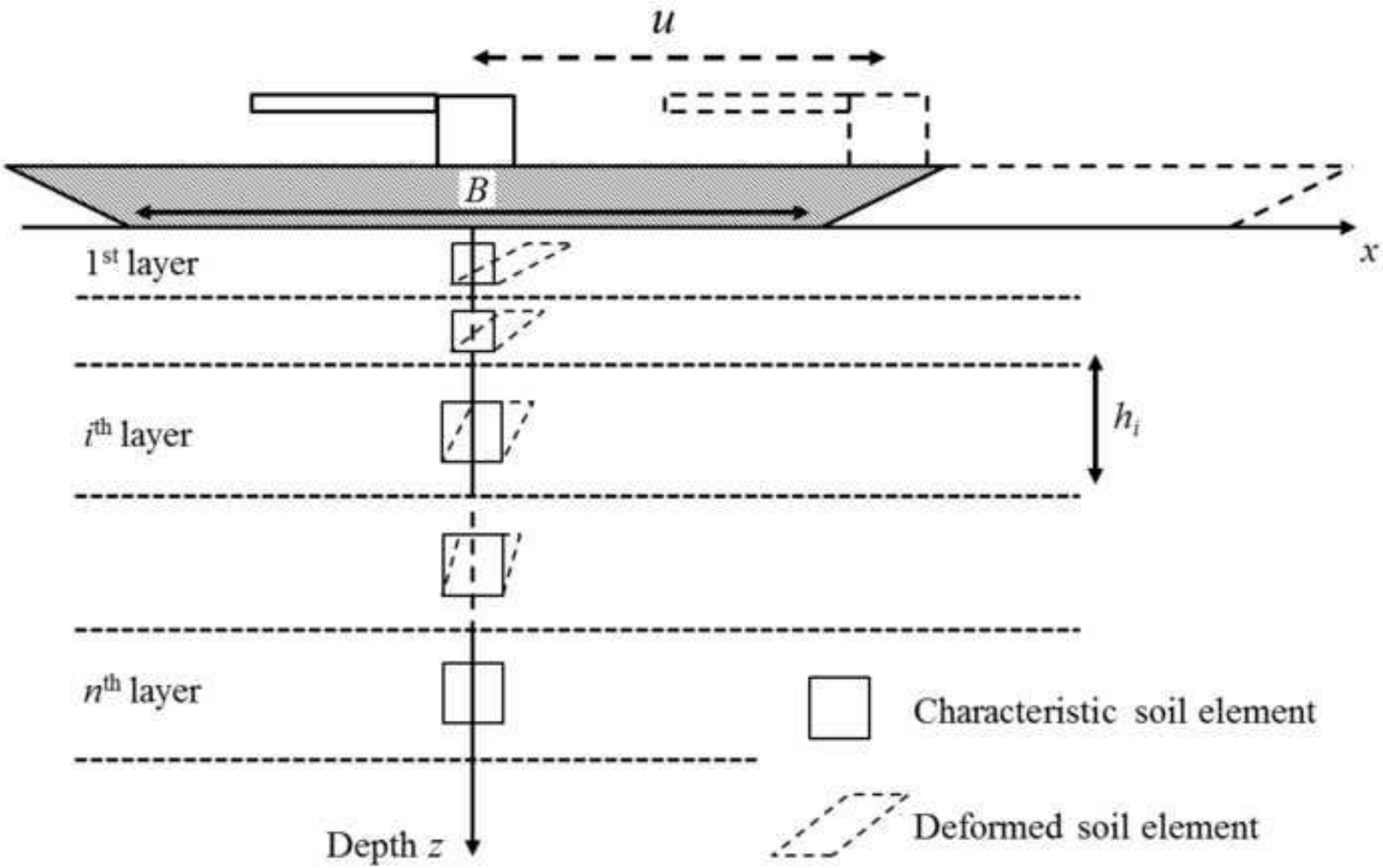

Figure 4

Click here to download high resolution image

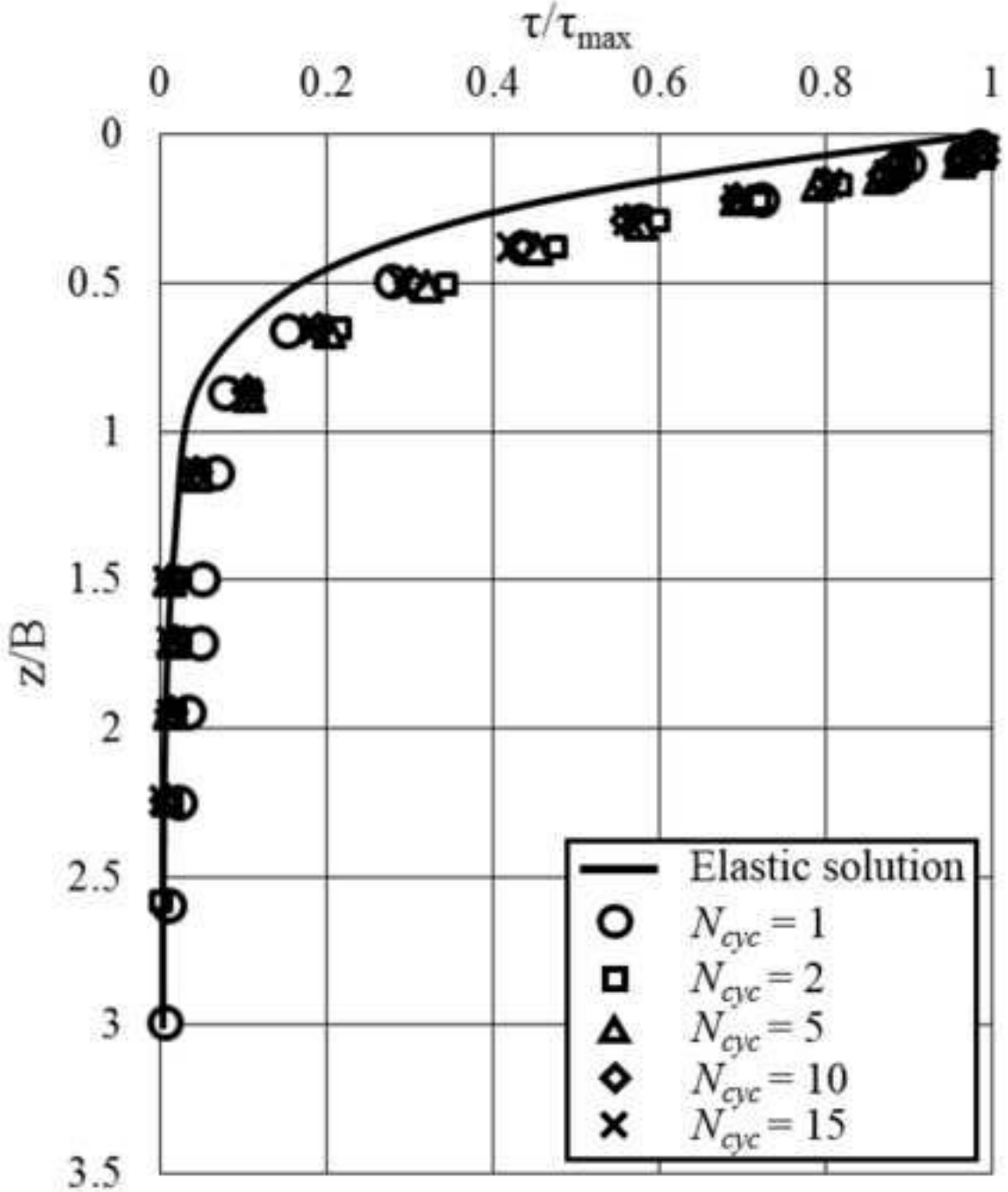

Figure 5

Click here to download high resolution image

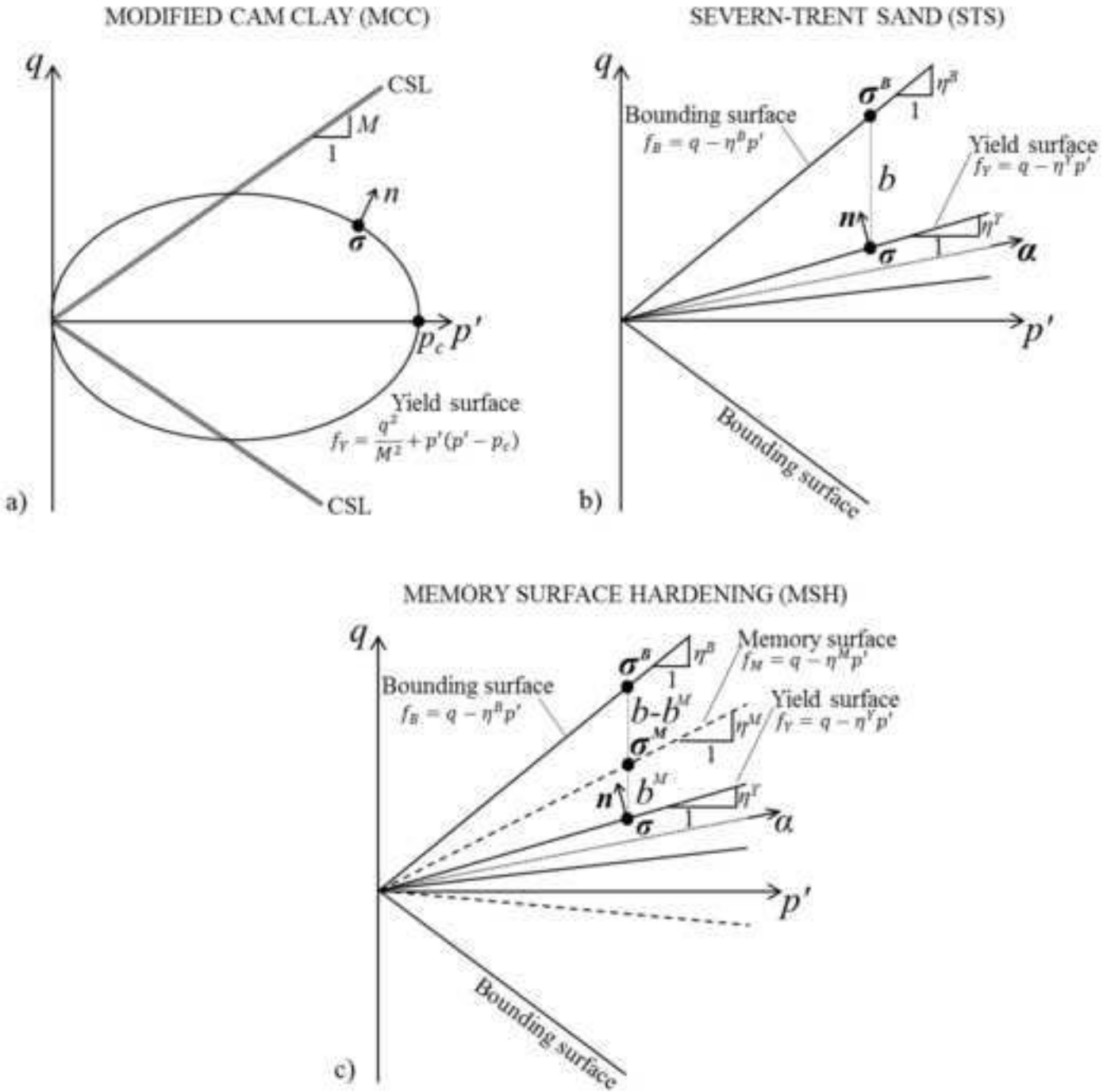

Figure 6
Click here to download high resolution image

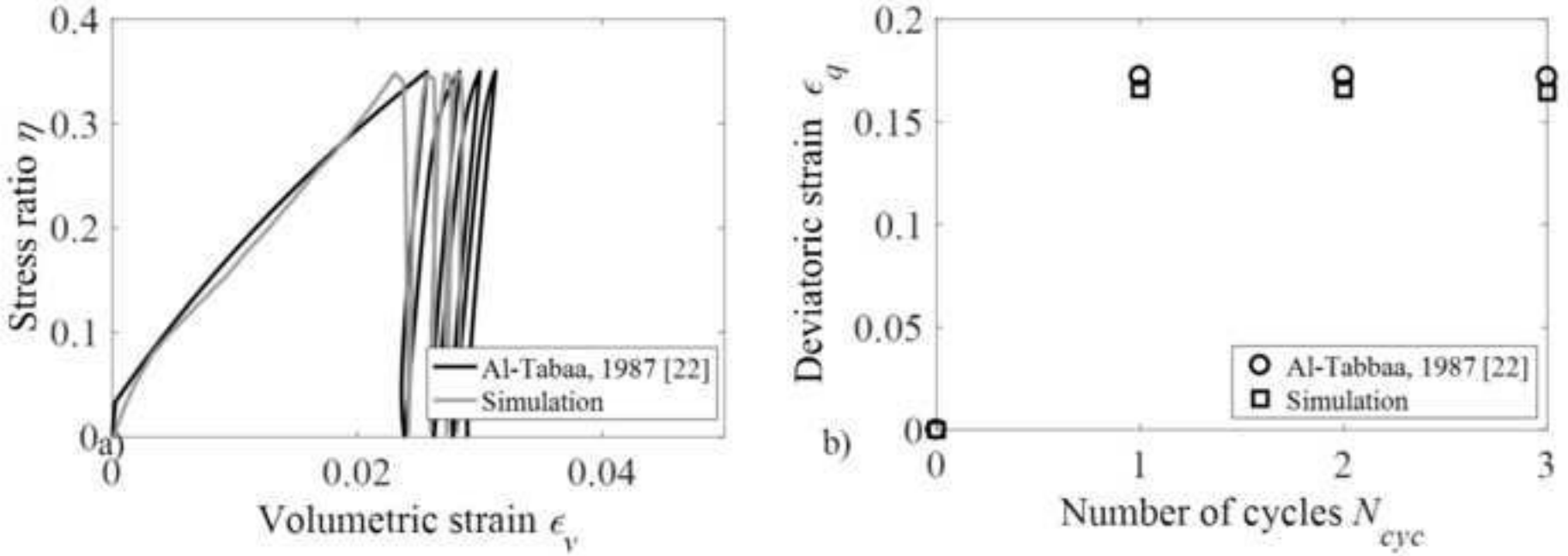

Figure 7
Click here to download high resolution image

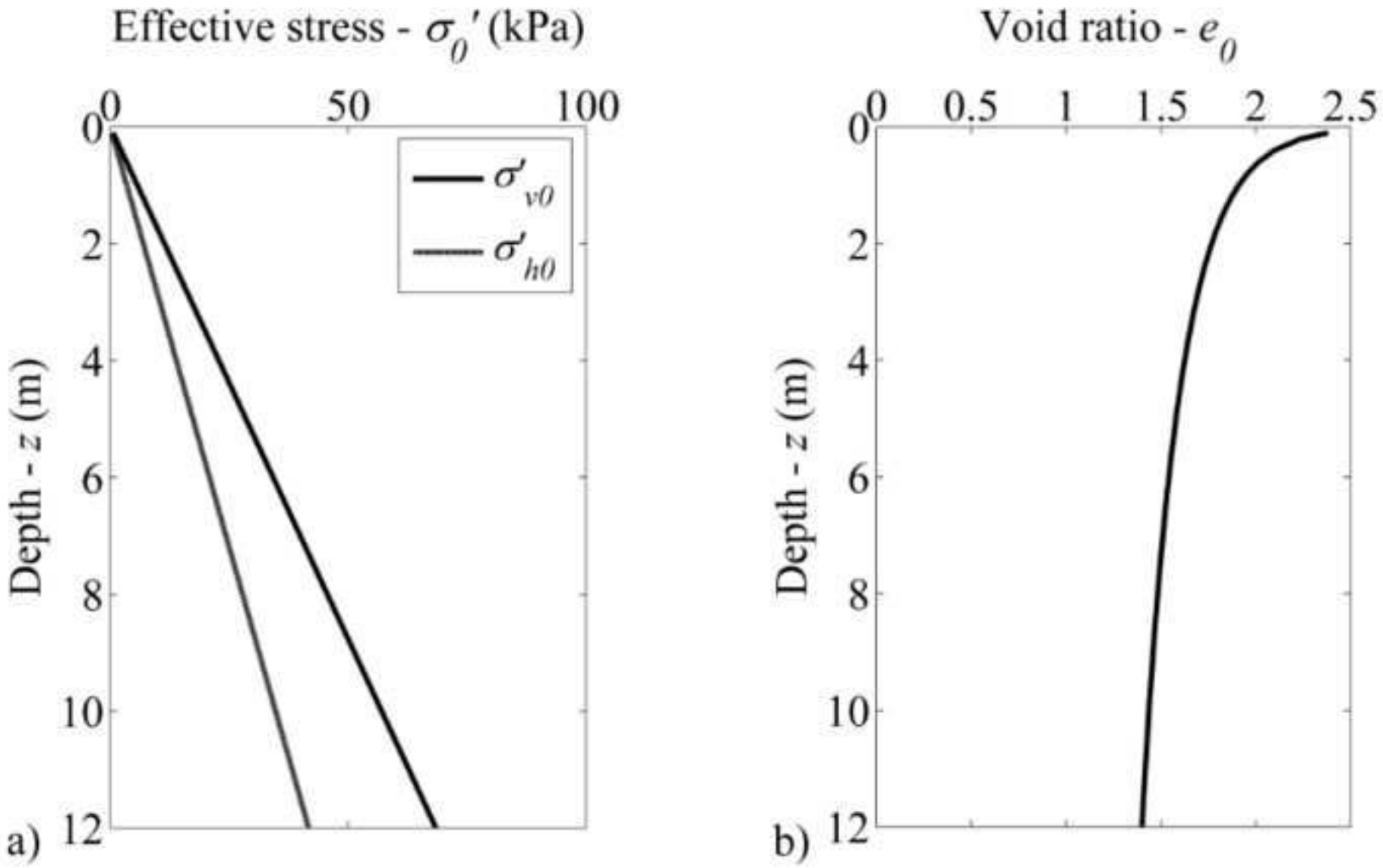

Figure 8

Click here to download high resolution image

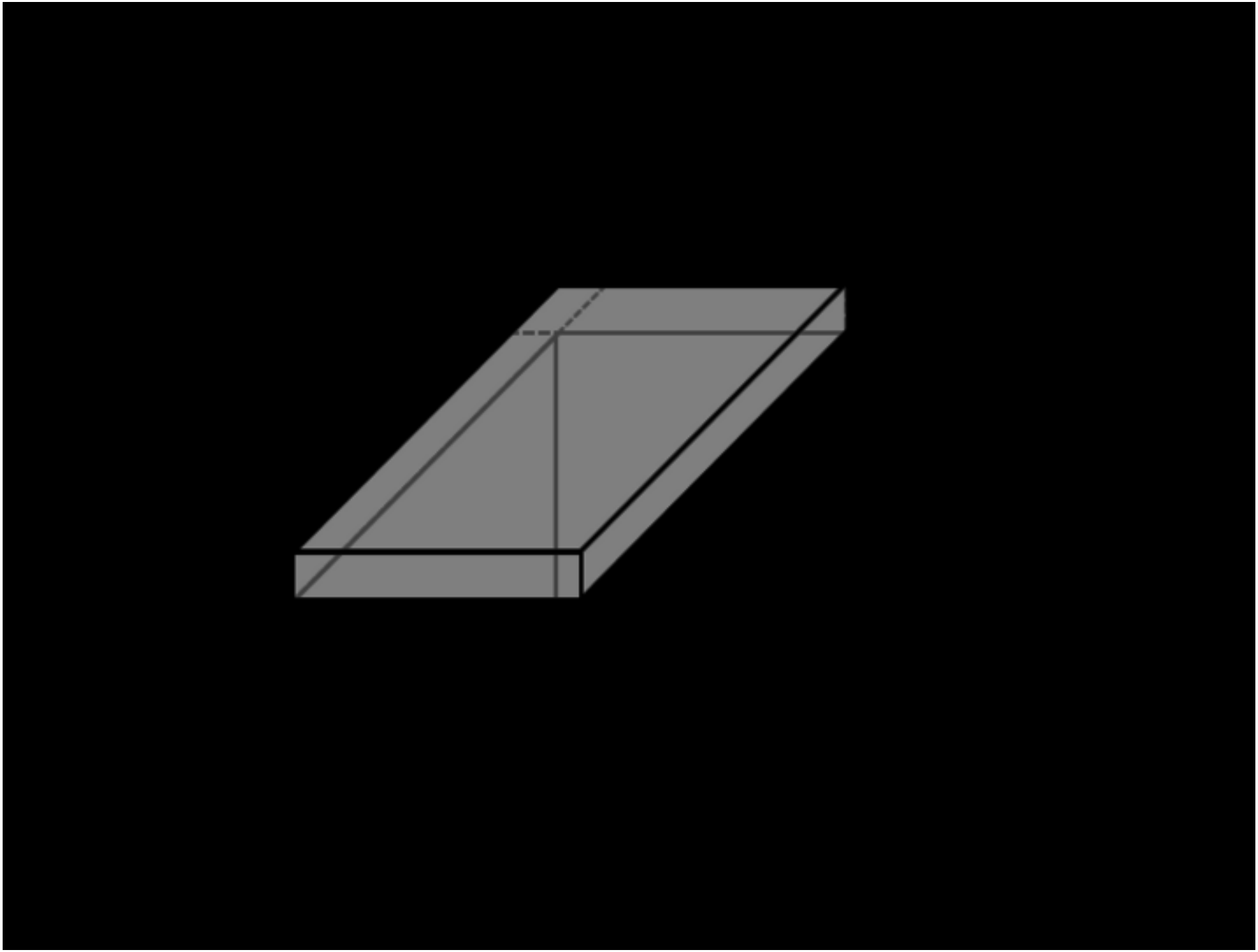

Figure 9
Click here to download high resolution image

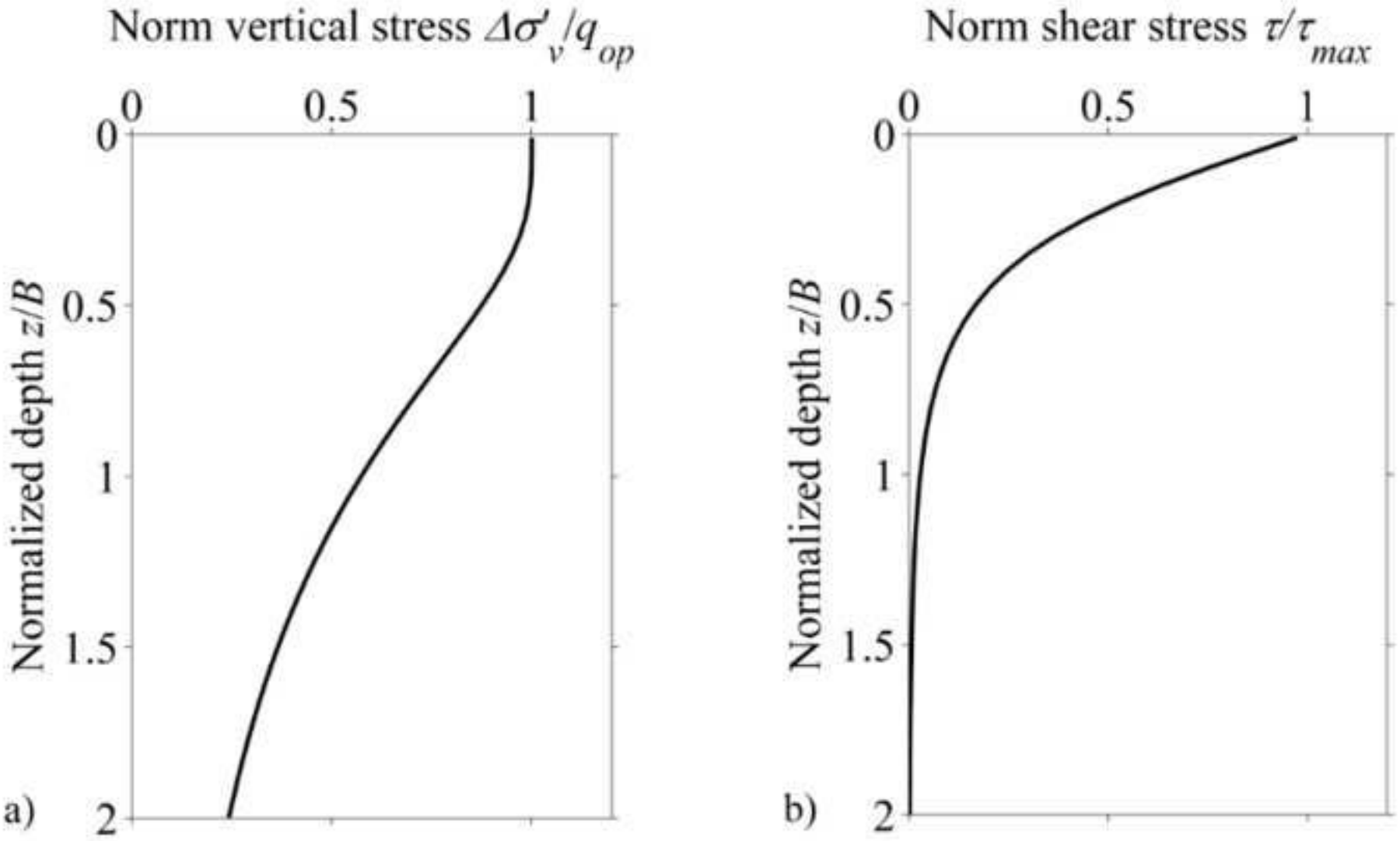

Figure 10

Click here to download high resolution image

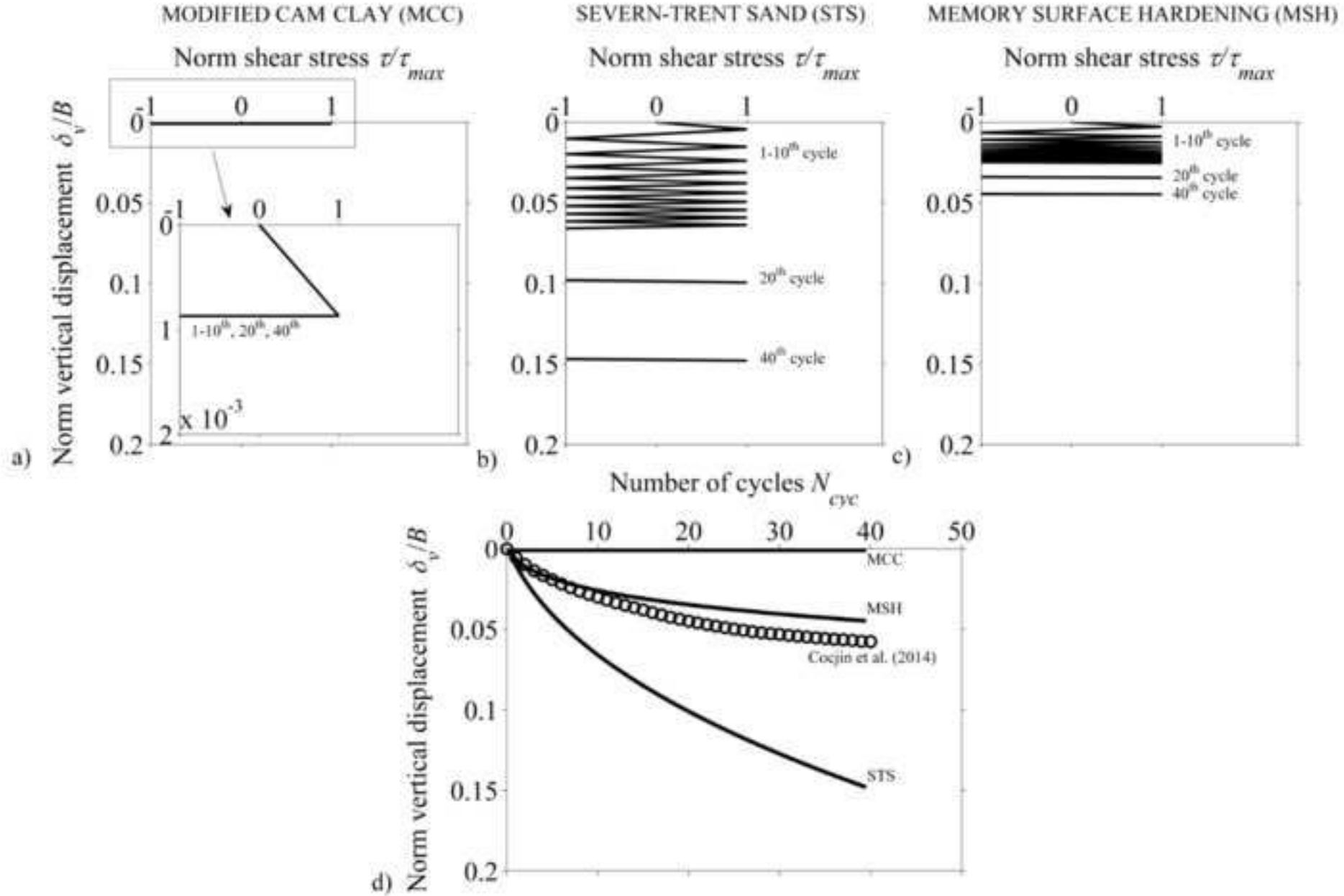

Figure 11
Click here to download high resolution image

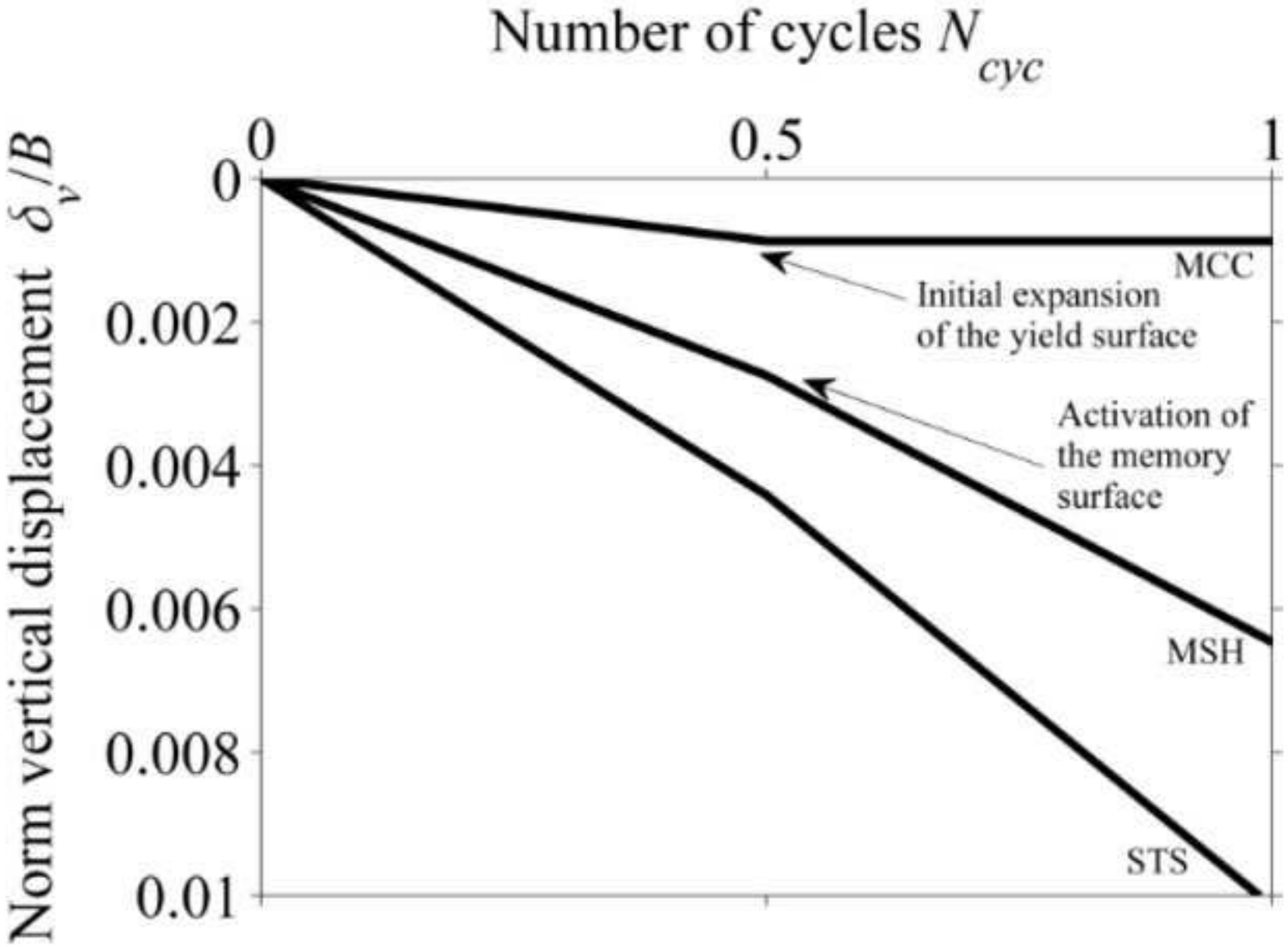

Figure 12
Click here to download high resolution image

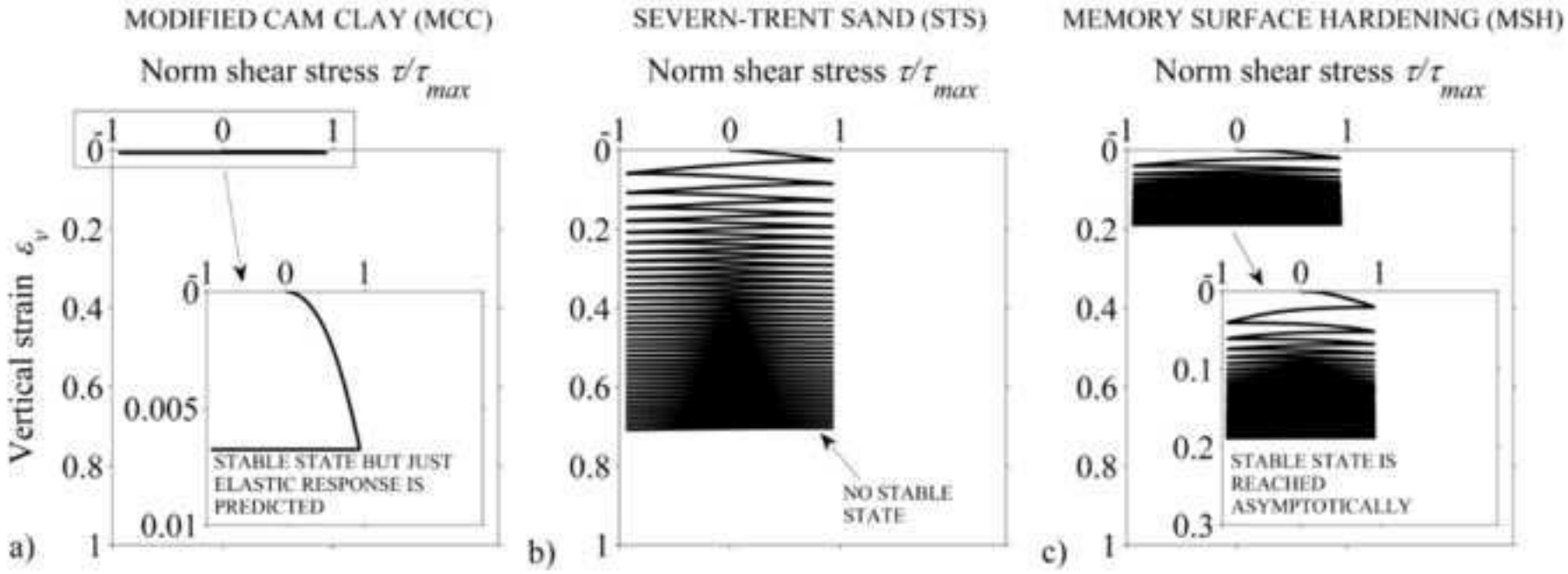

Figure 13

Click here to download high resolution image

Figure 14
Click here to download high resolution image

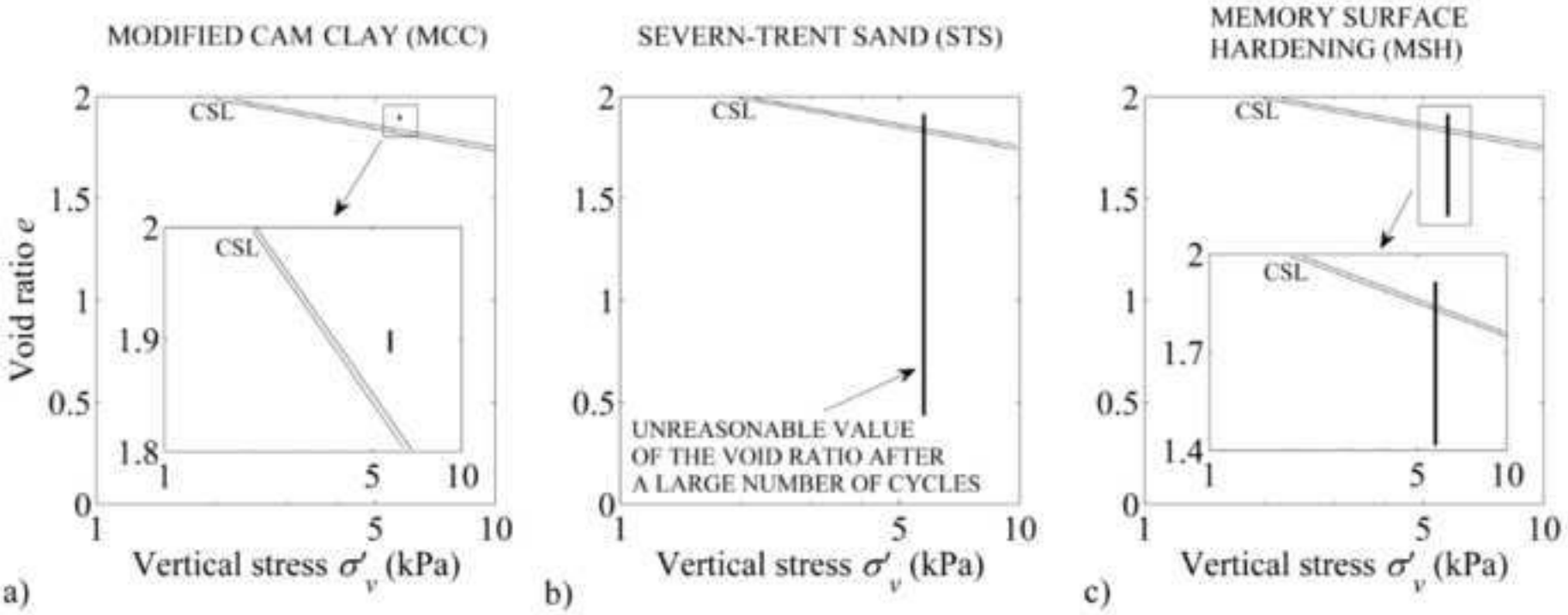

Figure 15

Click here to download high resolution image

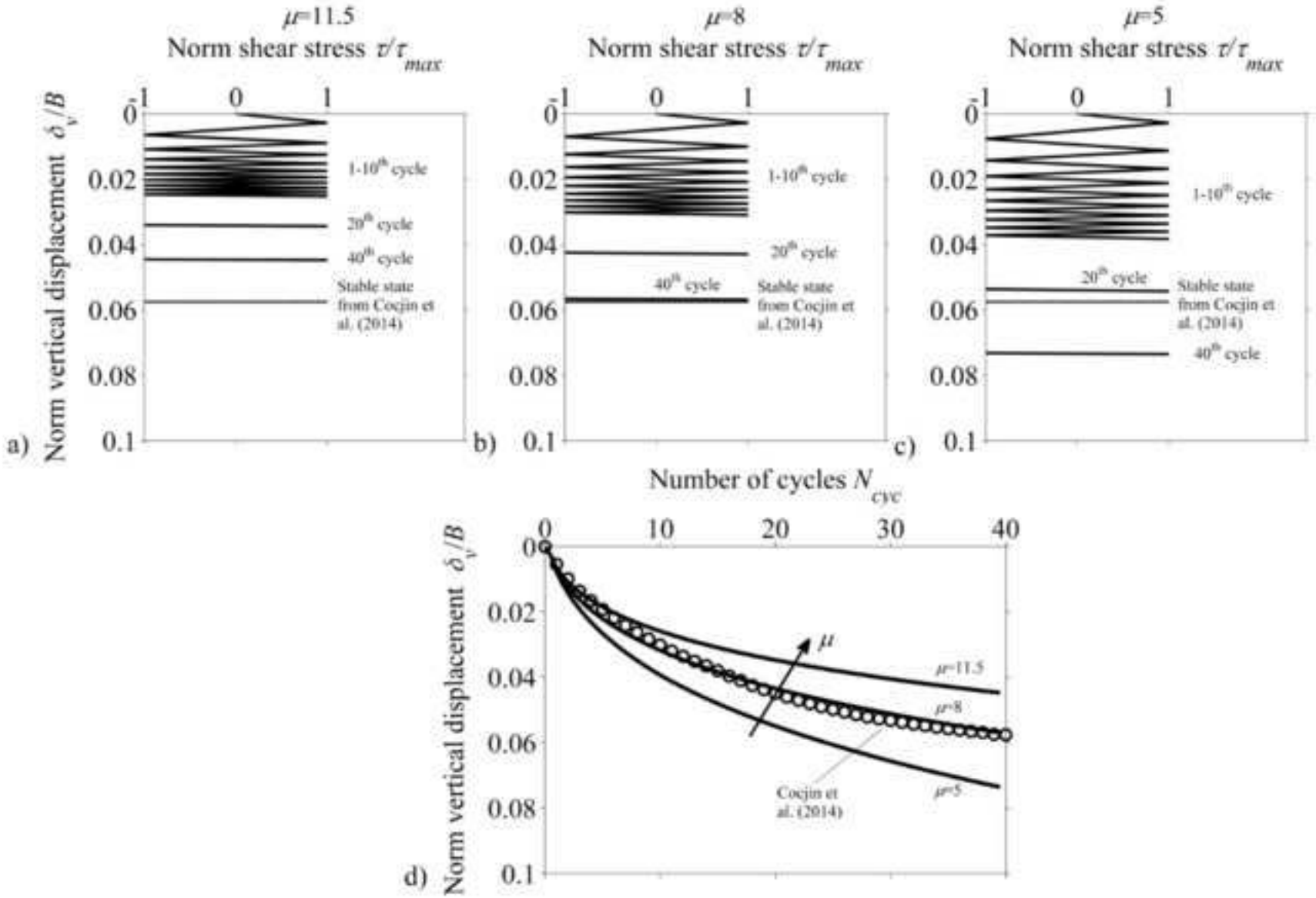

Figure 16
Click here to download high resolution image

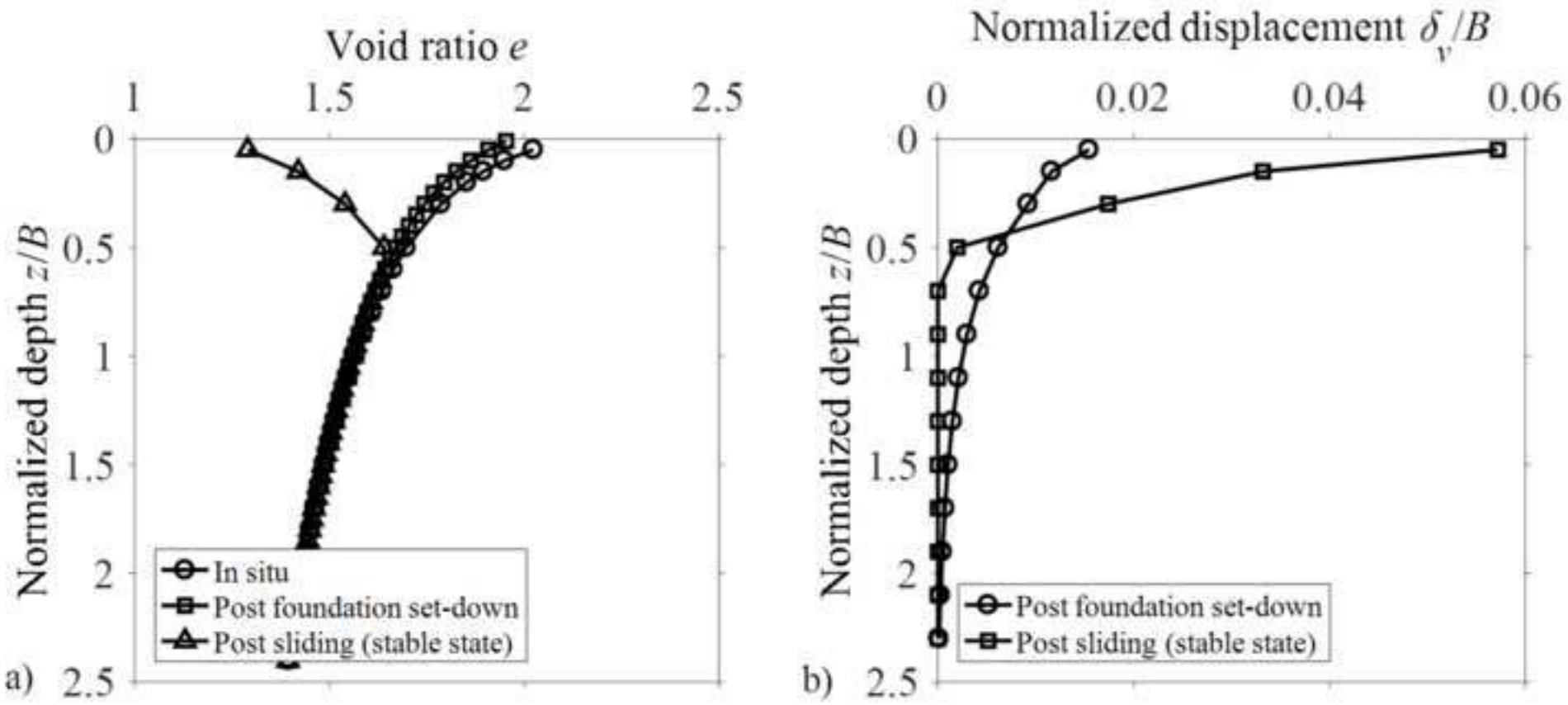

Figure 17
Click here to download high resolution image

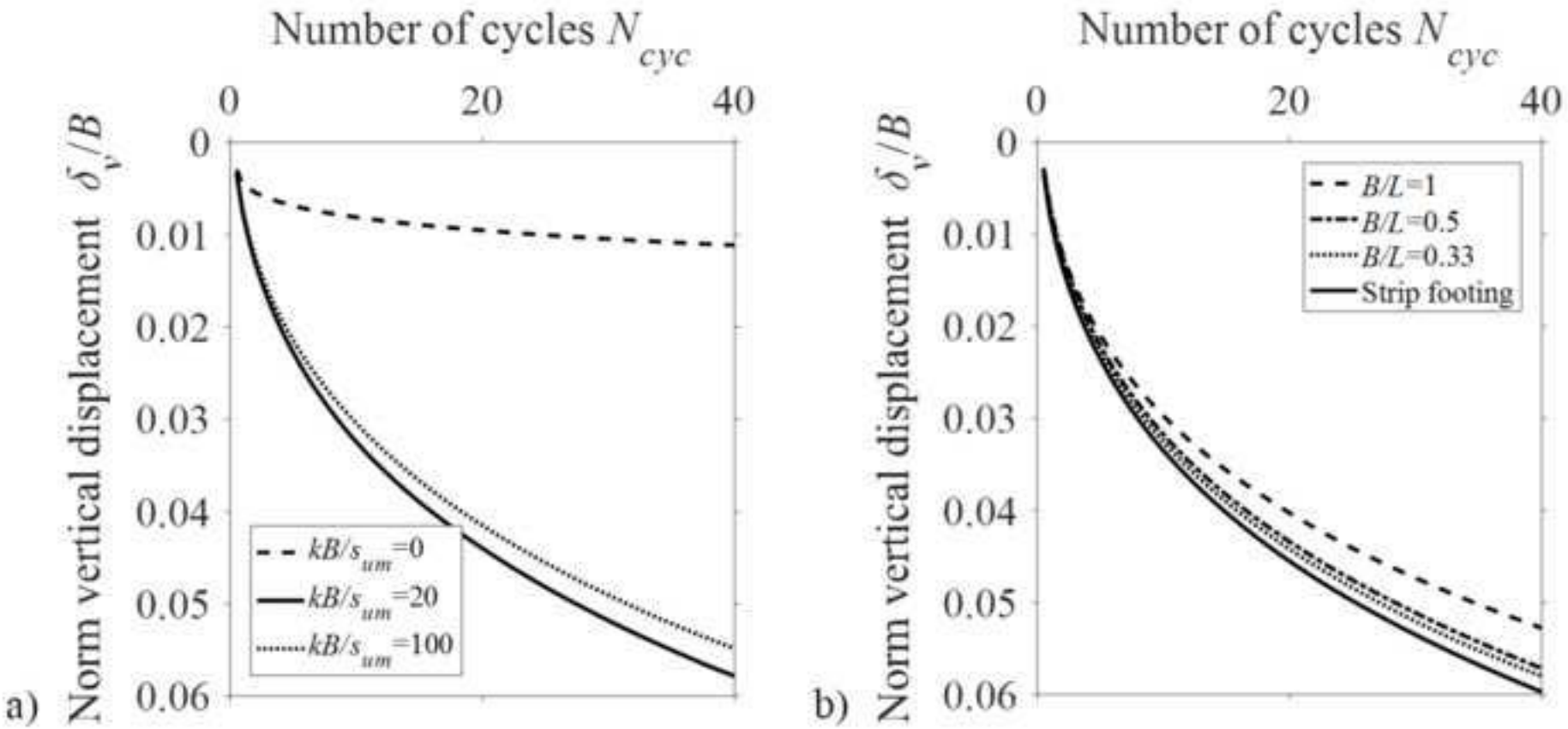

Table of figures